Kr environment in feldspathic glass and melt: A high pressure, high temperature X-ray absorption study

Celine Crepisson, Chrystèle Sanloup, Laurent Cormier, Marc Blanchard,
Jessica Hudspeth, Angelika D Rosa, Olivier Mathon, Tetsuo Irifune

1 **Kr environment in feldspathic glass and melt: a high pressure, high**

2 **temperature X-ray absorption study**

3

4 **Céline Crépisson[a*], Chrystèle Sanloup[a], Laurent Cormier[b], Marc Blanchard[c], Jessica**

5 **Hudspeth[a], Angelika D. Rosa[d], Olivier Mathon[d], Tetsuo Irifune[e]**

6

7 [a]Sorbonne Université, CNRS, UMR 7193 - Institut des Sciences de la Terre de Paris (ISTeP),

8 4 place Jussieu, 75005, Paris, France

9

10 [b]Sorbonne Université, CNRS UMR 7590, MNHM, IRD, Institut de Minéralogie de Physique

11 des Matériaux et de Cosmochimie (IMPMC), 75005 Paris, France

12

13 [c]Géosciences Environnement Toulouse (GET), Université de Toulouse, CNRS, IRD, UPS, 14

14 avenue Edouard Belin, 31400 Toulouse, France

15

16 [d]European Synchrotron Radiation Facility, ESRF, 71 Avenue des Martyrs, 38000 Grenoble, 6

17 France.

18

19 [e]Ehime University, Geodynamic Research Center, Matsuyama, Japan

20

21 [*]Corresponding author. Address : Céline Crépisson, Institut des Sciences de la Terre de Paris

22 (ISTeP), Sorbonne Université, Case 110, 4 place Jussieu, 75005 Paris, France. Tel.: +33 1 44

23 27 60 64. Email : celine.crepisson@upmc.fr

24

25

Abstract

Noble gases are used to trace the evolution of the Earth's atmosphere and magmatic processes. However little is known about their solubility mechanisms in silicate melts or glasses, whereas it could be fundamental to interpret these data. We report here the first *in situ* X-ray absorption spectroscopy data at the Kr K-edge on a feldspathic Kr-bearing glass and melt (0.5 wt % Kr) up to 2.7 GPa and 1086°C. Kr fitting of the EXAFS signal shows that Kr is surrounded by oxygen atoms. Two Kr-O distances are identified: 2.49±0.1 Å and 3.32±0.1 Å. Results can be interpreted as two Kr populations. Kr surrounded by O atoms at 3.32±0.1 Å suggests a filling of the large cavities available in the silicate network, in agreement with previous studies. On the contrary, Kr surrounded by O atoms at 2.49±0.1 Å, and the observed + 0.6 eV shift of the edge position at high pressure, suggest Kr bonding to O atoms and Kr oxidation inside cages formed by the largest aluminosilicate rings (i.e. ~ 12-membered-rings). Present results show that heavy noble gases incorporation in silicate melts can no longer be considered as a passive filling of the voids.

1. Introduction

Due to their supposed chemical inertia, high volatility, and high dilution, noble gases have been intensively studied by geochemists to understand the formation of the Earth's atmosphere, and to study mantle dynamics. None of Kr stable isotopes (^{78,80,82,83,84,86}Kr) is

2

51 purely radiogenic, and Pu and U fission yields are very low for Kr. Thus Kr cannot be used to

52 constrain chronology of the atmosphere evolution, and as such has been less studied than He,

53 Ne, Ar, and Xe. However, the small amount of radiogenic Kr makes it suitable to trace air

54 component in fluid inclusions (Böhlke and Irwin, 1992). Earth atmospheric Kr isotope

55 composition, unchanged since at least 3.3 Ga (Avice et al., 2017), falls in-between solar and

56 chondritic compositions (Pepin, 1991). Kr isotopic ratios in CO_2 magmatic well gases that

57 probed the continental lithosphere, showed a significant enrichment in ^{84}Kr and ^{86}Kr

58 compared to the atmosphere (Holland et al., 2009). The discovery of Kr isotopic fractionation

59 in these well gases, taken as a proxy of deep mantle gases, was interpreted as the signature of

60 a primordial Kr chondritic component (Holland et al., 2009). Nevertheless Holland et al.

61 (2009) argue that early degassing of an accreted primordial chondritic composition, followed

62 by mass fractionation during atmosphere loss, fails to explain the composition of the modern

63 atmosphere. Instead, late accretion of cometary material is assumed to explain Kr isotope

64 signature of the atmosphere. Although very few samples have been analyzed for all Kr

65 isotopes, mantle-derived basalts (MORBs, OIBs) have an atmospheric Kr isotopic

66 composition (Moreira et al., 1998; Trieloff et al., 2000; Graham, 2002). This homogeneous

67 composition could be due to atmospheric Kr recycling at subduction zones (Holland and

68 Ballentine, 2006).

69   To explain highly precise Kr isotopic data, geochemists need an understanding of Kr

70 behavior in silicate melts, including Kr solubility value and mechanism, as well as Kr degree

71 of compatibility.

72   Fractionated fission Kr has also been observed in the Okhlo natural nuclear reactor. In

73 nuclear plants, ^{85}Kr is a common fission product. Nuclear waste confinement by vitrification

74 in SiO_2-rich glasses has been used for many years (Ojovan and Lee, 2011). Accumulation of

75 Kr leads to the formation of nanobubbles where pressure may reach 2.6 GPa (Martin et al.,

76   2015) under high temperature generated by irradiation. Understanding of Kr behavior in

77   silicate glasses is thus crucial for long nuclear waste storage.

78   The majority of studies dedicated to noble gases solubility in melts are based on

79   analyses of recovered glassy samples, and did not directly investigate the noble gas structural

80   environment in the silicate network, as noble gases can escape from the silicate structure at

81   ambient conditions. These studies showed that noble gas solubility decreases with increasing

82   radius (from He to Xe) (Caroll and Stolper, 1993, Lux, 1987, Shibata et al., 1998), and that

83   this solubility strongly depends on the chemical composition of the melt. Noble gas solubility

84   was first related to ionic porosity, i.e. the absolute volume of voids (Caroll and Stolper, 1993),

85   whereas Shibata et al. (1998) showed that it was better inversely correlated to the number of

86   non-bridging oxygen per silicon, even if the presence of Al may modify this trend (Bouhifd

87   and Jephcoat, 2006). Based on these findings and noble gas relative chemical inertia, noble

88   gases were supposed to passively fill the voids of the silicate network.

89   *In situ* structural data on the environment of heavy noble gases in silicate melts and

90   glasses are scarce. Wulf et al. (1999) performed an X-ray absorption study at the Kr K-edge in

91   a SiO_2 glass (1.97 wt % Kr). They identified a Kr-O distance of 3.45±0.1 Å, interpreted as

92   corresponding to a local rearrangement of the silicate network into a local clathrasil-type

93   environment around the Kr atom. The supposed chemical inertia of Kr and Xe, the most

94   reactive of the noble gases, has been questioned throughout the past 15 years, with the

95   synthesis of numerous Kr and Xe compounds (see Grochala, 2007 for a review). Bonding of

96   Xe to O in compressed haplogranitic magmas had also been evidenced by *in situ* X-ray

97   diffraction (Leroy et al. 2018).

98   In the present study, we perform *in situ* X-ray absorption spectroscopy (XAS) at the

99   Kr K-edge, to specifically access Kr structural environment in a feldspathic (sanidine) glass.

4

100   Starting $(Na,K)AlSi_3O_8$ glass composition was chosen as representative of the

101   chemistry of a major mineral of the continental crust, and proxy of silica-rich melts that can

102   be generated at pressure reaching 2 GPa in orogenic contexts (Jimenez-Munt et al., 2008), and

103   in subduction contexts from melting of hydrous basalt (Prouteau et al., 2001), or silica-rich

104   sediments (Turner et al., 2012). Experiments were conducted at pressures (P) and

105   temperatures (T) up to 2.7 GPa and 1086°C, relevant for both continental crust melting and

106   subduction zone contexts.

107

108   **2.Material and Methods**

109

110   **2.1 Sample: synthesis and characterization**

111

112   The starting glass of Kr/Xe-bearing sanidine was synthesized in a piston cylinder press

113   at 3.5 GPa and 1400°C for 24 hours before quenching. For this purpose, Xe and Kr were

114   loaded as a 1:1 gaseous mix along with sanidine powder in a Pt capsule (Boettcher et al.,

115   1989). Sanidine is a high-temperature feldspar, of atomic composition $(K_xNa_{1-x})AlSi_3O_8$ with

116   x higher than 0.32 (Bendel and Schmidt, 2008). In our experiments, sanidine powder was

117   obtained by grinding a natural sanidine mineral $(K_{0.52}Na_{0.43}Al_{1.05}Si_{2.96}O_8$, formula unit

118   retrieved from electron microprobe analysis) from the Sorbonne Université mineralogical

119   collection.

120   Starting glass and recovered sample were mounted in epoxy, polished and C-coated.

121   They were observed by Scanning Electron Microscope (SEM) with a Zeiss Supra 55

122   (equipped with a field emission gun). Detection of Xe and Kr was optimized with an

123   acceleration voltage of 20 keV and a working distance of 6.6 mm in backscatter mode.

124   Electron microprobe analyses (EMPA) were done on a CAMECA SX5, at CAMPARIS centre

125   at Sorbonne Université. Operating conditions were 15 kV accelerating voltage, 10 nA beam

126   current, and a focused beam for point analysis. We use the method from Montana et al. (1993)

127   for Kr, which was calibrated by measuring the counts on neighboring elements (i.e. Rb). Xe

128   was calibrated using a known standard analyzed by Particle-Induced X-ray Emission (data

129   published in Leroy et al., 2018).

130   The synthesized starting glass is chemically homogeneous (based on SEM and EMP

131   analyses) with presence of Kr/Xe gas bubbles indicating that saturation was reached. Contents

132   of 2.2 wt % Xe (0.36 at %) and 0.5 wt % Kr (0.13 at %) were measured by electron

133   microprobe analyses from an average of seven points of analysis in areas free of micrometric

134   gas bubbles. Average composition in wt % of the starting glass is given in Table 1. Recovered

135   sample was quenched from 1040°C and 2.7 GPa, where it reequilibrated as partial melt and

136   feldspar crystals (Figure 1), following cooling from fully molten state (1415°C and 3 GPa)

137   which was reached with the initial purpose to collect XAS data at the Xe-edge. Kr and Xe are

138   only observed in the glass, with striking alignments of Kr/Xe gas nanobubbles (Figure 1).

139   Average analyses of the recovered sample are given in Table 1, although degassing upon

140   quenching prevents Xe and Kr contents to be determined by EMP analysis.

141

142   **2.2 Experimental set-up**

143

144   *In-situ* X-ray absorption spectroscopy (XAS) was performed on beamline BM23 at the

145   ESRF, dedicated to general purpose XAS (Mathon et al., 2015). High pressure and

146   temperature conditions up to 2.7 GPa and 1086°C (Table 2) were generated in a Paris

147   Edinburgh Press (Besson et al., 1992). We used a cell assembly developed by Kono et al.

148   (2014) and adapted from Yamada et al. (2011). More details on the cell-assembly and

149 experimental set-up can be found in Rosa et al. (2016). The sample (0.75 mm diameter and

150 1.5 mm height) was encapsulated in a synthetic nanopolycrystalline diamond (NPD) cylinder

151 caped with Pt-Rh caps. The use of NPD prevents glitches from a single or polycrystalline

152 diamond capsule, which deteriorate the XAS signal. Temperature was determined using

153 calibration from Kono et al. (2014), and pressure using unit cell volume of hBN from the cell

154 assembly (based on X-ray diffraction measurements) and equation of state from Le Godec et

155 al. (2000). Error bars are ±50°C for temperature and ±0.2 GPa for pressure.

156

157 **2.3 XRD and XAS measurements**

158

159 Angle-resolved X-ray diffraction data were recorded on a MAR165 CCD at 15 keV.

160 Image plates were integrated using Fit 2D software (Hammersley, 1997). Cell parameters of

161 hBN were determined using POWDER CELL software (Kraus and Nolze, 1996).

162 XAS transmission measurements were performed first at the Kr K-edge (14326 eV) up to 2.7

163 GPa, upon increase of temperature up to 1086°C, and upon decrease of temperature down to

164 505°C, before quenching to room temperature (Table 2). Xe K-edge spectra were recorded

165 following measurement at the Kr K-edge upon increasing temperature up to 1415°C and 3

166 GPa, and upon cooling to 1040°C at 2.7 GPa followed by quenching. Xe K-edge spectra are

167 however not of sufficient quality to allow fitting, given the very small absorption jump (0.09

168 compared to 0.25 at the Kr K-edge), and are thus not shown here. Energy calibration of the

169 edge position was made by frequent analyses of Kr gaseous standards. The beam size on the

170 sample was 300 x 80 μm². Transmitted X-ray intensity was recorded by ionization chambers

171 filled with gaseous Ar-He mixed gas. Signal was collected from 14244 eV to 14971 eV at the

172 Kr K-edge (451 points analysis). Counting times, number of scans, and P/T conditions are

173   given in Table 2. Energy steps were adapted as a function of the edge position, each scan

174   takes about 1 hour.

175

176   **2.4 Processing of XAS data**

177

178   The edge of the standard was fixed to 14326 eV, and the edge of each sample was

179   recalibrated using the averaged edge value of two gaseous Kr standards taken before and after

180   the sample measurement. For Kr standard, no significant shift of the Kr K-edge was noted

181   (0.4 eV at the largest). After correction of edge position, data were cut at 14800 eV for better

182   normalization.

183   Data processing was performed using ATHENA and ARTEMIS packages, based on the

184   IFEFFIT programs (Ravel and Newville, 2005). Each scan was corrected with a pre-edge and

185   a post-edge baseline. Position of the edge was determined by the position of the first

186   derivative of the absorption. The intensity of the jump at the edge was then normalized to one.

187   After merging of the scans collected at a given P/T condition, data were corrected using a

188   background function. We used an automated background subtraction method (AUTOBKG)

189   developed by Newville (Newville, 2001) and implemented in the ATHENA software. This

190   correction minimizes the features below the first atom-atom distance in the R-space. R_{bkg} was

191   fixed to 1.2 Å.

192   To fit the data at the Kr K-edge, we used a k-range of ~ 2.2-6.5 Å^{-1} (Table 3), due to low

193   signal to noise ratio at higher k values. A small k-range ensures that all the different

194   contributions to the Fourier transform are not artifacts but really arise from neighboring

195   atoms. Real part of backward Fourier transform was exported to ARTEMIS software to be

196   fitted using R-range ~ 1.1-3.8 Å (Table 3). Fitting made on real part of backward Fourier

197   transform ensures that all XANES and noise contributions are removed from the EXAFS

signal. Fit parameters include: amplitude reduction factor (S0), average distances of the

neighboring atom to the central Kr atom, Debye Waller factor (σ^2), and difference of edge

position compared to standard value (ΔE_0). ΔE_0 values remain smaller than 7 eV, attesting

consistency of the fits. It was necessary to add a third order anharmonic cumulant expansion

fitting parameter (C3) for high pressure or high temperature measurements (Stern et al, 1991;

Farges et al., 1994). C3 is a measure of the asymmetry of the signal disorder, which arises in

glasses from configurational disorder associated to thermal vibration at high pressure and/or

high temperature conditions. The absolute value of C3 remains smaller than 0.009 $\mathring{A}^3$, similar

to values found by Cochain et al. (2015) on silicate glasses and melts at high pressure and

temperature conditions. As no Kr standard was analyzed in the course of the experiment

besides Kr gas, it is not possible to determine coordination numbers (CN). We therefore fixed

S0 at a common value of 0.79, and fixed the value of CN. In total, seven parameters must be

fitted (first interatomic distance, σ^2 and C3 for the two contributions and ΔE_0) whereas N, the

number of variables to fit, cannot exceed (Teo, 1986):

$$N = \frac{2\Delta R \Delta k}{\pi} \qquad (1)$$

In our case $\Delta k \approx 4.3 \ \mathring{A}^{-1}$ and $\Delta R \approx 2.8 \ \mathring{A}$. Therefore maximum number of parameters N,

which can be fitted is ~ 7.7, indicating that we can theoretically fit our data as exposed above.

3.Results and Discussion

3.1. XAS data at the Kr K-edge

222   XAS data were recorded at ambient conditions, at high pressure and high temperature, and

223   after quenching (Table 2). Potassic sanidine ($KAlSi_3O_8$) is expected to melt around 1500°C at

224   2.6-2.7 GPa (Boettcher et al., 1984). Reports on the $KAlSi_3O_8$-$NaAlSi_3O_8$ join under

225   anhydrous conditions at 1 atm showed that melting temperature of $KAlSi_3O_8$ drops by 100°C

226   for our starting composition ($Na_{0.43}K_{0.52}Al_{1.05}Si_{2.96}O_8$, atomic formula retrieved from EMPA)

227   (Schairer, 1950). Glass transition temperature (Tg) of felspathic glass at 1 atm was found in-

228   between 907-948°C based on viscosity measurements (Petermann et al., 2008; Richet and

229   Bottinga, 1984). Moreover, viscosity is shown to decrease from 0 GPa to 2.5 GPa for both

230   sanidine melt (White and Montana, 1990) and albite melt (Kushiro, 1978). Thus Tg is

231   expected to be even lower than 907-948°C at our pressure conditions. Therefore our

232   measurements at 1086°C (and potentially at 920°C) were recorded above Tg and before

233   recrystallization, i.e. on the supercooled liquid, behaving like a melt. Well-defined oscillations

234   are visible in the X-ray absorption signal, and clearly differ from the signature of Kr gas and

235   Kr liquid under pressure (Di Cicco et al., 1996) (Figures 2 and 3).

236   Rapid damping of the EXAFS signal indicates disorder beyond the first shell. We

237   compare in Figure 3 our data with the k^2-weighted EXAFS function recorded at 27°C on UO_2

238   (8 at % Kr) previously implanted with Kr ions (Martin et al., 2015). Oscillations observed

239   after 4 $Å^{-1}$ clearly differ from our data sets. The magnitude of the Fourier transform (k-range

240   used is displayed in Table 3) clearly shows two peaks at all measurement conditions (Figure

241   4), indicating that two distances contribute to the signal, with the main distance at ~ 1.9 Å,

242   while Martin et al. (2015) reports a main distance at 3.44 Å. Kr environment in sanidine glass

243   is therefore different from that observed by Martin et al. (2015) in UO_2, i.e. Kr nanoclusters.

244   There is no noticeable change in the room temperature glass with pressure: data at ambient

245   pressure and after quenching at 1.4 GPa being similar (Figures 2, 3 and 4). The relative

246   intensity of the two peaks however varies with temperature, the magnitude of the Fourier

247   transform (Figure 4) being different at ambient temperature, at 505°C and 706°C, and

248   especially in the melt at 920°C and 1086°C.

249

250   **3.2 Resolving Kr environment in sanidine glass and melt**

251

252   Variations of fitted Kr-O distances over our experimental P/T range are within error

253   (i.e. ±0.1 Å). We thus evaluate averaged Kr-O distances for the whole P/T range, two Kr-O

254   distances are identified at 2.49±0.1 Å and 3.32±0.1 Å (Table 3, Fig. 5). No other neighboring

255   atom than oxygen could fit the observed XAS signal, although we considered other atomic

256   pairs such as Kr-Kr, Kr-Si, Kr-Na, or Kr-K. Identified distances confirm the absence of Kr

257   neighbors. Indeed Kr-Kr distance in solid cubic Kr is 3.68 Å at 2 GPa and room temperature

258   (Di Cicco et al., 1996). We can interpret these results as two distinct populations of Kr located

259   in two different sites of the silicate network. Results clearly differ from Wulf et al. (1999),

260   who only reported a Kr-O distance at 3.45 Å, as shown in Figure 5.

261   At ambient condition, there is no non-bridging oxygen in sanidine glass ($KAlSi_3O_8$),

262   and Al coordination number is four for all Al atoms (Thompson et al., 2011). Study of an

263   albite glass ($NaAlSi_3O_8$) quenched from the melt at 2.6 GPa showed that less than 3% of Al

264   atoms present a coordination number of five, whereas all remaining Al atoms have a

265   coordination number of 4 (Gaudio et al., 2015). Sanidine glass is thus fully polymerized, with

266   all Na^+/K^+ compensating the charge deficit created by the presence of Al^{3+} in tetrahedral

267   position. Molecular dynamic simulations showed that in soda aluminosilicate glass, for

268   Na/Si=1, distribution of the aluminosilicate rings at ambient pressure varies from 2 to 13

269   membered-rings, with 6 or 7 membered-rings being the most present ring population (Xiang

270   et al., 2013). Similarly, at ambient pressure, a ring size distribution from 2 to 12-membered

271   rings is predicted for silica glass with 6 to 7 membered-rings being the dominant ring

272   population (Kohara et al. 2011; Guerette et al., 2015). To our knowledge, no pore size

273 distribution data is available for our glass composition. Based on the similarity of ring size

274 distribution between aluminosilicate and silica glass, we assume that size of cages within

275 aluminosilicate rings range from 0.9 Å to 5.9 Å in diameter, like in silica glass (Guerette et

276 al., 2015). This size distribution indicates the presence of 5-5.9 Å-diameter voids, inside the

277 largest (i.e. ~ 12-membered) aluminosilicate rings. The Kr-O distance of 2.49±0.1 Å is

278 therefore compatible with a Kr atom located inside the largest observed rings of the silicate

279 network. This Kr-O distance falls in-between the sum of covalent radii of Kr and O (1.16 Å

280 and 0.66 Å respectively (Cordero et al., 2008)) and the sum of ionic radii of Kr^0 and O^{2-}

281 (respectively 1.78 Å for a coordination number of 6 (Zhang et al. 1995) and 1.4 Å (Shannon,

282 1976)). This result indicates that Kr is interacting closely with the neighboring oxygen atoms,

283 suggesting an oxidation of Kr. Under pressure, the edge position shifts by + 0.6 eV (Figure 6).

284 Shift of the edge can be related to change in the oxidation state as observed for Cu, Co, Fe,

285 Mn (e.g. Klysubun et al., 2015). This observation further supports a change in Kr oxidation

286 due to Kr-O bonding. Kr is in the oxidation state II in most of Kr compounds synthesized,

287 such as KrF_2, KrF^+ or $Kr_2F_3^+$ (Grosse et al., 1963, Burbank et al., 1972, Lehmann et al., 2001).

288 Kr oxidation number is expected to increase compared to gaseous Kr, if Kr is surrounded by

289 several O atoms.

290 The Kr-O distance of 3.32±0.1 Å cannot correspond to the presence of Kr atoms inside

291 aluminosilicate rings, as the size distribution is limited to 5.9 Å in diameter. This larger Kr-O

292 distance is similar to the 3.45±0.1 Å distance reported in SiO_2 glass at ambient pressure and 5

293 K (Wulf et al., 1999), and close to predictions from first principle molecular dynamics. Zhang

294 et al. (2009) indeed found Kr-O = 3.5 Å in liquid silica, with Kr coordination number varying

295 from 10 to 15 depending on pressure. Similar result was found by Guillot and Sator (2012)

296 using molecular dynamics with Kr-O = 3.45 Å in silica melt and 3.31 Å in rhyolite melt. This

297 large distance can be explained by the formation of large cavities in the melt where noble

298   gases are accommodated, in agreement with a passive filling of the void space, or with a

299   clathrasil-like environment (Wulf et al., 1999). Contribution of Kr fluid to this longer distance

300   cannot be ruled out if the few Kr bubbles observed on starting and quenched samples are not

301   fully homogenized with the melt at high pressure and temperature.

302   Disappearance of the larger Kr-O distance at higher temperatures (Figure 4), indicates

303   that smaller Kr-O distance is more favorable, possibly with the increase of Kr reactivity.

304   Moreover, the Debye Waller factor associated with the smallest Kr-O distance ($\sigma^2 1$), is twice

305   larger at room temperature than at high temperature (Table 3), suggesting that ordering of the

306   smaller Kr-O environment is higher. Measurements at high pressures and temperatures are all

307   above Kr melting point, whereas measurement after quenching at 1.4 GPa is below Kr

308   melting point (Ferreira and Lobo, 2008). Kr reactivity therefore seems enhanced above Kr

309   melting curve, suggesting that it is pressure-induced, i.e. it favors smaller volume, as observed

310   for Xe incorporation in olivine (Sanloup et al., 2011). Besides, the larger Kr-O distance

311   vanishes in the melt, i.e. at 920°C and 1086°C (Figure 4), indicating structural changes

312   between the melt and the glass. A complementary explanation could be a contribution of Kr

313   fluid to the longer Kr-O distance, which would diminish with temperature due to the increase

314   of Kr solubility in the melt.

315   Current knowledge of glass and silicate melt structures therefore supports the

316   hypothesis of two Kr populations, with one population of Kr, oxidized and possibly located in

317   the largest aluminosilicate rings, and one population filling the large cavities available in the

318   silicate network.

319

320   **4.Conclusion**

321

322 The present work provides evidence for the reactivity of Kr with silicate that adds up to the

323 previously reported evidences of Kr reactivity (Grochala, 2007). Kr oxidizes in feldspathic

324 glass and melt at high P/T conditions as shown by creation of short Kr-O bonds (2.49±0.1 Å)

325 and shift of the edge position. Kr behavior in compressed magmas thus appears to be

326 intermediate between that of an inert noble gas (He, Ne, Ar) and that of the heavier Xe.

327 Indeed Xe is shown to fully oxidize in compressed haplogranitic melts with Xe in the most

328 abundant 6-membered rings containing 12 nearest O, Xe-O distance of 2.05±0.05 Å is

329 similar to distance reported for covalent Xe-O bond in crystalline silicates (Probert, 2010;

330 Kalinowski et al., 2014; Crépisson et al., 2018). Both results question the supposed passive

331 filling of the void spaces by heavy noble gases (Caroll and Stolper, 1993; Shibata et al.,

332 1998), and the assumption that all noble gases can be considered as zero-charge cation (e.g.

333 Brooker et al., 2003).

334 Creation of short Kr-O bonds in sanidine melt at depth, supports the role of Kr recycling at

335 subduction zones, proposed by Holland and Ballentine (2006), as Kr will efficiently dissolve

336 in the melt. Hydrated melts will now need to be studied to test the influence of water, which is

337 thought to dramatically increase noble gases solubility (Nuccio and Paonita, 2000).

338 The Earth's atmosphere is depleted in heavy Kr isotopes compared to chondrites (Holland et

339 al., 2009). Observation of short Kr-O bonds in silicate melt, implying Kr reactivity, suggests

340 potential isotopic fractionation during partial-melting and melt percolation, as shown for

341 instance for Cu (Huang et al., 2017), and / or during fluid / melt interactions either upon fluid

342 injection at depth in subduction zones or degassing during magma ascent. This phenomenon

343 could have contributed to enrichment of well gases from the continental lithosphere in heavy

344 Kr isotopes, while most of the samples from the Earth's mantle (OIBs and MORBs) have an

345 atmospheric Kr isotopic composition due to intense recycling.

346

354

355

356

357

358

359

360

361

362

363

364

365

366

367

368

369

370

371

372 **References:**

373 Avice G., Marty B., and Burgess R. 2017. The origin and degassing history of the Earth's

374 atmosphere revealed by Archean xenon. Nature communications, 8, 15455.

375 Bendel V. and Schmidt B.C. 2008. Raman spectroscopic characterisation of disordered alkali

376 feldspars along the join $KAlSi_3O_8$–$NaAlSi_3O_8$: application to natural sanidine and

377 anorthoclase. European Journal of Mineralogy, 20, 1055–1065.

378 Besson J.M., Hamel G., Grima T., Nelmes R.J., Loveday J.S., Hull S., and Häusermann D.

379 1992. A large volume pressure cell for high temperature. High Pressure Research, 8, 625-630.

380 Boettcher A., Guo Q., Bohlen S., and Hanson B. 1984. Melting in feldspars-bearing systems

381 to high pressures and the structures of aluminosilicate liquids. Geology, 12, 202-204.

382 Boettcher S.L., Guo Q., and Montana A. 1989. A simple device for loading gases in high-

383 pressure experiments. American Mineralogist, 74, 1383-1384.

384 Böhlke J.K. and Irwin J.J. 1992. Brine history indicated by argon, krypton, chlorine, bromine,

385 and iodine analyses of fluid inclusions from the Mississippi Valley type lead-fluorite-barite

386 deposits at Hansonburg, New Mexico. Earth and Planetary Science Letters, 110, 51-66.

387 Bouhifd A. and Jephcoat A.P. 2006. Aluminium control of Argon solubility in silicate melts

388 under pressure. Nature, 439, 961-964.

389 Brooker R.A., Du Z., Blundy J.D., Kelley S.P., Allan N.L., Wood B.J., Chamorro E.M.,

390 Wartho J.A., Purton J.A. 2003. The 'zero charge' partitioning behaviour of noble gases during

391 mantle melting. Nature. 423, 6941, 738-741.

392 Burbank R.D., Falconer W.E., and Sunder W.A. 1972. Crystal Structure of Krypton

393 Difluoride at -80°C. Science, 178, 1285-1286.

394 Carroll M.R. and Stolper E.M. 1993. Noble gas solubilities in silicate melts and glasses: New

395 experimental results for argon and the relationship between solubility and ionic porosity.

396 Geochimica et Cosmochimica Acta, 57, 5039-5051.

397 Cochain B., Sanloup C., De Grouchy C., Crépisson C., Bureau H., Leroy C., Kantor I., and

398 Irifune T. 2015. Bromine speciation in hydrous silicate melts at high pressure. Chemical

399 Geology, 404, 18-26.

400 Cordero B., Gomez V., Cremades E., Alvarez S. 2008. Covalent radii revisited. Dalton

401 Transactions, 2832-2838.

402 Crépisson C., Blanchard M., Balan E., and Sanloup C. 2017. New constraints on Xe

403 incorporation mechanisms in olivine from First-principles calculation, Geochimica et

404 Cosmochimica Acta.

405 Di Cicco A., Filipponi A., Itié J-P., and Polian A. 1996. High-pressure EXAFS measurements

406 of solid and liquid Kr. Physical Review B, 54, 9086-9098.

407 Farges F., Brown G.E., Calas G., Galoisy L., and Waychuna G.A. 1994. Structural

408 transformation in Ni-bearing $Na_2Si_2O_5$ glass and melt. Geophysical Research Letters, 21,

409 1931-1934.

410 Ferreira A.G.M., and Lobo L.Q. 2008. The fusion curves of xenon, krypton, and argon. The

411 Journal of Chemical Thermodynamics, 40, 618–624.

412 Gaudio S.J., Lesher C.E., Maekawa H., and Sen S. 2015. Linking high-pressure structure and

413 density of albite liquid near the glass transition. Geochimica et Cosmochimica Acta, 157, 28–

414 38.

415 Graham D.W. 2002. Noble gas isotope geochemistry of Mid-Ocean Ridge Basalt and Ocean

416 Island Basalts: characterization of mantle source reservoirs. in *Noble gases in Geochemistry*

417 *and Cosmochemistry*, Reviews in Mineralogy and Geochemistry, 247-318.

418   Grochala W. 2007. Atypical compounds of gases, which have been called 'noble'. Chemical

419   Society Reviews, 36, 1632-1655.

420   Grosse, A.V., Kirshenbaum, A.D., Streng, A.G, and Streng L.V. 1963. Krypton Tetrafluoride:

421   Preparation and Some Properties. Science, 139, 1047-1048.

422   Guerette M., Ackerson M.R., Thomas J., Yuan F., Watson E.B., Walker D., and Huang L.

423   2015. Structure and Properties of Silica Glass Densified in Cold Compression and Hot

424   Compression. Nature Scientific Reports, 5.

425   Guillot B., and Sator N. 2012. Noble gases in high-pressure silicate liquids: A computer

426   simulation study. Geochimica et Cosmochimica Acta, 80, 51-69.

427   Hammersley A. 1997. FIT2D: An Introduction and Overview. Technical Report

428   No.ESRF97HA02, ESRF.

429   Holland G., and Ballentine C. 2006. Seawater subduction controls the heavy noble gas

430   composition of the mantle. Nature, 441, 186-191.

431   Holland G., Cassidy M., and Ballentine C.J.. 2009. Meteorite Kr in Earth's Mantle Suggests a

432   Late Accretionary Source for the Atmosphere. Science, 326, 1522-1525.

433   Huang J., Huang F., Wang Z., Zhang X., Yu H. 2017. Copper isotope fractionation during

434   partial melting and melt percolation in the upper mantle: Evidence from massif peridotites in

435   Ivrea-Verbano Zone, Italian Alps. Geochimica et Cosmochimica Acta, 211, 48-63.

436   Jiménez-Munt I., Fernandez M., Vergés J., and Platt J.P. 2008. Lithosphere structure

437   underneath the Tibetan Plateau inferred from elevation, gravity, and geoid anomalies. Earth

438   and Planetary Science Letters, 267, 276-289.

439   Kalinowski J., Rasanen M., Gerber R.B. 2014. Chemically-bound xenon in fibrous silica.

440   Physical Chemistry Chemical Physics, 16, 11658–11661.

441   Klysubun W., Hauzenberger C.A., Ravel B., Klysubun P., Huang Y., Wongtepa W.,and

442   Sombunchoo P. 2014. Understanding the blue color in antique mosaic mirrored glass from the

443   Temple of the Emerald Buddha, Thailand. X-ray spectrometry, 44, 116-123.

444   Kohara S., Akola J., Morita H. , Suzuya K., Weber J.K.R., Wilding M.C., and Benmore C.J.

445   2011. Relationship between topological order and glass forming ability in densely packed

446   enstatite and forsterite composition glasses. PNAS, 108, 14780-14785.

447   Kono Y., Park C., Kenney-Benson C., Shen G., and Wang Y. 2014. Toward comprehensive

448   studies of liquids at high pressures and high temperatures: Combined structure, elastic wave

449   velocity, and viscosity measurements in the Paris–Edinburgh cell. Physics of the Earth and

450   Planetary Interiors, 228, 269-280.

451   Kraus W. and Nolze G. 1996. POWDER CELL - a program for the representation and

452   manipulation of crystal structures and calculation of the resulting X-ray powder patterns.

453   Journal of Applied Crystallography, 29, 301-303.

454   Kushiro I. 1978. Viscosity and structural changes of albite ($NaAlSi_3O_8$) melt at high

455   pressures. Earth and Planetary Science Letters, 41, 87-90.

456   Le Godec Y., Solozhenko V.L., Mezouar M., Besson J-M., and Syfosse G. 2000. In situ X-ray

457   diffraction studies of formation of cubic and hexagonal graphite-like boron nitride by the

458   reaction of elemental boron with supercritical hydrazine. Science and Technology of High

459   Pressure. Universities Press, Hyderabad, India, 2, 1031-1034.

460   Lehmann J.F., Dixon D.A., and Schrobilgen G. 2001. X-ray Crystal Structures of alpha-KrF2,

461   [KrF][MF6] (M=As, Sb, Bi), Kr2F3][SbF6].KrF2, [Kr2F3]2[SbF6]2.KrF2, and

462   Kr2F3][AsF6] .[KrF][AsF6]; Synthesis and Characterization of [Kr2F3][PF6].nKrF2; and

463   Theoretical Studies of KrF2, KrF+, Kr2F3+, and the [KrF][MF6](M = P, As, Sb, Bi) Ion

464   Pairs. Inorganic Chemistry, 40, 3002-3017.

465   Leroy C. Sanloup C., Bureau H., Schmidt B.C., Konopkova Z., Raepsaet C. 2018. Bonding of

466   xenon to oxygen in magmas at depth. Earth and Planetary Science Letters, accepted.

467   Lux G. 1987. The behavior of noble gases in silicate liquids: Solution, diffusion, bubbles and

468   surface effects, with applications to natural samples. Geochimica et Cosmochimica Acta, 31,

469   1549-1560.

470   Martin P.M., Vathonne E., Carlot G., Delorme R., Sabathier C., Freyss M., Garcia P.,

471   Bertolus M., Glatzel P., and Proux O. 2015. Behavior of fission gases in nuclear fuel: XAS

472   characterization of Kr in UO_2. Journal of Nuclear Materials, 466, 379-392.

473   Mathon O., Beteva A., Borrel J., Bugnazet D., Gatla S., Hino R., Kantor I., Mairs T., Munoz

474   M., Pasternak S., Perrina F., and Pascarelli S. 2015. The time-resolved and extreme

475   conditions XAS (TEXAS) facility at the European Synchrotron Radiation Facility: the

476   general-purpose EXAFS bending-magnet beamline BM23. Journal of synchrotron radiation,

477   22, 1548-1554.

478   Meshik A.P., Kehm K., Hohenberg C.M. 2000. Anomalous xenon in zone 13 Okelobondo.

479   Geochimica et Cosmochimica Acta, 64, 9, 1651-1661.

480   Montana A., Guo Q., Boettcher S., White B.S., and Brearley M. 1993. Xe and Ar in high-

481   pressure silicate liquids. American Mineralogist, 78, 1135-1142.

482   Moreira M., Kunz J., and Allègre J.C. 1998. Rare gas systematics in popping rock: Isotopic

483   and elemental compositions in the upper mantle. Science, 279, 1178-1181.

484   Newville M. 2001. EXAFS analysis using FEFF and FEFFIT. Journal of Synchrotron

485   Radiation, 8, 96-100.

486   Nuccio P.M., and Paonita A. 2000. Investigation of the noble gas solubility in H2O-CO2

487   bearing silicate liquids at moderate pressure II: the extended ionic porosity (EIP) model. Earth

488   and Planetary Science Letters, 183, 499-512.

489   Ojovan M.I., and Lee W. E. 2010. Glassy wasteforms for nuclear waste immobilization.

490   Metallurgical and Materials Transactions A, 42, 4, 837-851.

491   Pepin R. 1991. On the origin and early evolution of terrestrial planet atmospheres and

492   meteoritic volatiles. Icarus, 92, 2–79.

493   Pertermann, M., Whittington, A.G., Hofmeister, A.M., Spera F.J., Zayak J. 2008. Transport

494   properties of low-sanidine single-crystals, glasses and melts at high temperature.

495   Contributions to Mineralogy and Petrology, 155, 689-702.

496   Probert, M.I.J. 2010. An ab initio study of xenon retention in α-quartz. Journal of Physics of

497   Condensed Matter, 22, 025501.

498   Prouteau, G., Scaillet, B., Pichavant, M., and Maury, R. 2001. Evidence for mantle meta-

499   somatism by hydrous silicic melts derived from subducted oceanic crust. Nature, 410, 6825,

500   197–200.

501   Ravel B., and Newville M. 2005. ATHENA, ARTEMIS, HEPHAESTUS: data analysis for X-

502   ray absorption spectroscopy using IFEFFIT. Journal of Synchrotron Radiation, 12, 537–541.

503   Richet P, and Bottinga Y. 1984. Glass transitions and thermodynamic properties of

504   amorphous SiO_2, $NaAlSi_nO_{2n+2}$ and $KAlSi_3O_8$. Geochimica et Cosmochimica Acta, 48, 3,

505   453-470.

506   Rosa A.D., Pohlenz J., de Grouchy C., Cochain B., Kono Y., Pasternak S., Mathon O.,

507   Irifune T., and Wilke M. 2016. *In-situ* characterization of liquid network structures at high

508   pressure and temperature using X-ray Absorption Spectroscopy coupled with the Paris-

509   Edinburgh press. High Pressure Research, 36, 332-347.

510   Sanloup C., Schmidt B.C., Gudfinnsson G., Dewaele A., and Mezouar M. 2011. Xenon and

511   Argon: a contrasting behavior in olivine at depth. Geochimica et Cosmochimica Acta, 75,

512   6271–6284.

513   Schairer J. F. 1950. The alkali-feldspar join in the system $NaAlSiO_4$-$KAlSiO_4$-SiO_2. The

514   Journal of Geology, 58, 512-517.

515   Shannon R.D. 1976. Revised effective ionic radii and systematic studies of interatomic

516   distances in halides and chalcogenides. Acta Crystallographica, A32, 751-767.

517   Shibata T., Takahashi E., and Matsuda J.I. 1998. Solubility of neon, argon, krypton, and

518   xenon in binary and ternary silicate systems: A new view on noble gas solubility. Geochimica

519   et Cosmochimica Acta, 62, 1241-1253.

520   Stern E.A., Livins P., and Zhang Z. 1991. Thermal vibration and melting from a local

521   perspective. Physical review B, 43, 8850-8860.

522   Thompson L.M. and Stebbins J.F. 2011. Non-bridging oxygen and high-coordinated

523   aluminum in metaluminous and peraluminous calcium and potassium aluminosilicate glasses:

524   High-resolution ^{17}O and ^{27}Al MAS NMR results. American Mineralogist, 96, 841–853.

525   Trieloff M., Kunz J., Clague D., Harrison D., and Allègre J.C. 2000. The nature of pristine

526   noble gases in mantle plumes. Science, 288, 5468, 1036-1038.

527   Turner, S., Caulfield, J., Turner, M., vanKeken, P., Maury, R., Sandiford, M., and Prouteau,

528   G. 2012. Recent contribution of sediments and fluids to the mantle's volatile budget. Nature

529   Geoscience, 5, 1, 50–54.

530   White B.S., and Montana A. 1990. The effect of H_2O and CO_2 on the viscosity of sanidine

531   liquid at high pressures. Journal of Geophysical Research: Solid Earth Banner, 95 (B10),

532   15683-15693

533   Wulf R., Calas G., Ramos A., Büttner H., Roselib K., and Rosenhauer M. 1999. Structural

534   environment of krypton dissolved in vitreous silica. American Mineralogist, 84, 1461–1463.

535   Xiang Y., Du J., Smedskjaer M.M., and Mauro J.C. 2013. Structure and properties of sodium

536   aluminosilicate glasses from molecular dynamics simulations. The Journal of Chemical

537   Physics, 139.

538 Yamada A., Wang Y., Inoue T., Yang W., Park C., Yu T., and Shen G. 2011. High-pressure

539 x-ray diffraction studies on the structure of liquid silicate using a Paris–Edinburgh type large

540 volume press. Review of Scientific Instruments, 82.

541 Zhang Y. and Xu Z.. 1995. Atomic radii of noble gas elements in condensed phases.

542 American Mineralogist, 80, 670-675.

543 Zhang L., Van Orman J.A., and Lacks D.J. 2009. Effective radii of noble gas atoms in silicate

544 from first principles molecular simulation. American Mineralogist, 94, 600-609.

545

546

547

548

549

550

551

552

553

554

555

556

557

558

559

560

561 *Table 1: Average composition of the starting glass (7 data points) and recovered sample (20*

562 *data points both in the glassy and crystalline parts) in oxide wt %, in brackets: standard*

563 *deviation.*

	Na$_2$O	SiO$_2$	Al$_2$O$_3$	K$_2$O	CaO	Xe	Kr	Total
Starting material	4.80 (0.2)	63.6 (0.40)	19.2 (0.14)	8.70 (0.24)	0.78 (0.05)	2.18 (0.04)	0.52 (0.05)	99.7 (0.47)
Recovered sample	2.9 (0.6)	65 (1)	19.8 (0.6)	11(1)	0.3 (0.2)	[0-1.3]*	[0-0.5]*	100(1)

564 ** due to degassing upon quenching Kr and Xe contents cannot be properly evaluated by*

565 *EMPA. Ranges of analyzed contents are given as an indication.*

566

567

568

569

570

571

572

573

574

575

576

577

578

579

580

581

582   *Table 2: P/T conditions and state of the sample for each XAS measurement. n.s = number of*

583   *scans, count. time = counting time per point analysis (451 point analysis).*

584

Kr K-edge				
P (GPa)	T (°C)	state	n.s	count. time
0	20	glass	7	2s
2.6	920	melt	4	2s
2.7	1086	melt	5	2s
2	706	glass	5	2s
2	505	glass	5	2s
1.4	20	quench	4	2s

585

586

587

588

589

590

591

592

593

594

595

596

597

598

599

600 *Table 3: Pressure-Temperature conditions and EXAFS-derived structural parameters.*

601 *Conservative error bars are ± 0.05 eV for ΔE_0, ± 0.1 Å for Kr-O distances and ± 0.05 Å² for*

602 *σ^2.*

603

P (GPa)	T (°C)	k-range (Å^{-1})	R-range (Å)	ΔE_0 (eV)
0	20	2.2 - 6.5	1.1 - 3.5	3.32
2.6	920	2.3 - 6.5	1.2 - 4.0	6.09
2.7	1086	2.3 - 6.5	1.1 - 3.8	7.00
2	706	2.3 - 6.5	1.1 - 3.5	6.45
2	505	2.3 - 6.5	1.1 - 3.8	5.84
1.4	20	2.2 - 6.5	1.1 - 4.0	3.50

P (GPa)	T (°C)	Kr-O1 (Å)	$\sigma^2 1$ (Å^2)	$C3_1$ (Å^3)
0	20	2.42	0.025	-
2.6	920	2.45	0.009	0.0021
2.7	1086	2.51	0.014	0.0078
2	706	2.53	0.009	0.0085
2	505	2.53	0.012	0.0076
1.4	20	2.49	0.021	0.0035

P (GPa)	T (°C)	Kr-O2 (Å)	$\sigma^2 2$ (Å^2)	$C3_2$ (Å^3)
0	20	3.38	0.048	-
2.6	920	3.27	0.040	-0.0090
2.7	1086	3.37	0.042	0.0090

2	706	3.34	0.064	-0.0034
2	505	3.29	0.045	-0.0090
1.4	20	3.30	0.049	-0.0057

604

605

606

607

608

609

610

611

612

613

614

615

616

617

618

619

620

621

622

623   *Figure 1: SEM images in backscatter mode of recovered sample after XAS measurements.*

624   *Feldspars recrystallized upon cooling to 1040°C at 2.7 GPa, coexisting with partial melt*

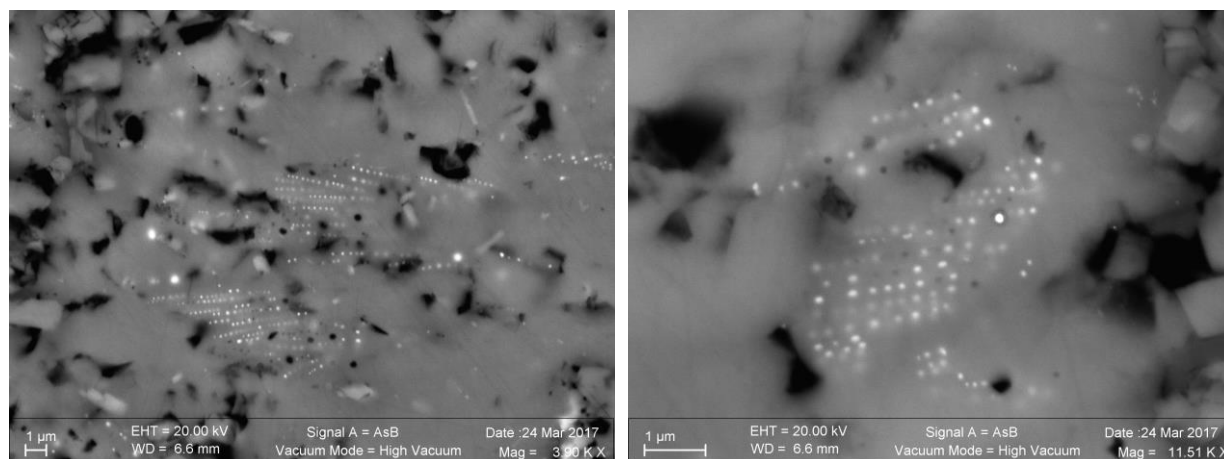625   *recovered as a glass upon quenching. Kr/Xe-nanobubbles (bright dots) are visible.*

626

627

628

629

630

631

632

633

634

635

636

637

638

639

640

Figure 2: Normalized X-ray absorption spectra for sanidine glass and supercooled liquid,

642   *gaseous Kr at ambient conditions, and liquid Kr at 0.75 GPa (Di Cicco et al., 1996).*

643

644
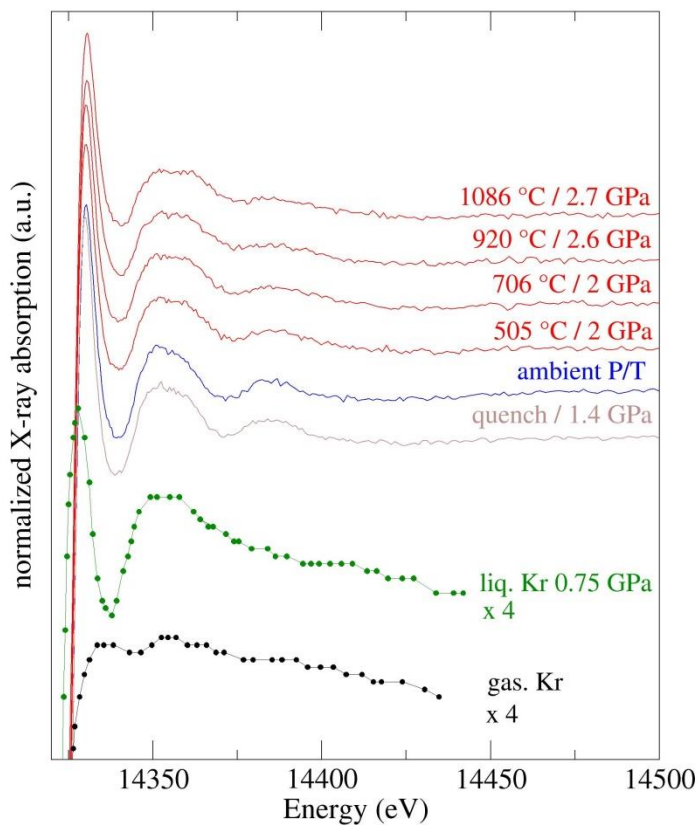
645

646

647

648

649

650

651

652

Figure 3: k^2-weighted EXAFS function for sanidine glass and supercooled liquid (color

coding: same as Figure 2), and for UO_2 at room conditions (Martin et al., 2015).

655

656

657

658

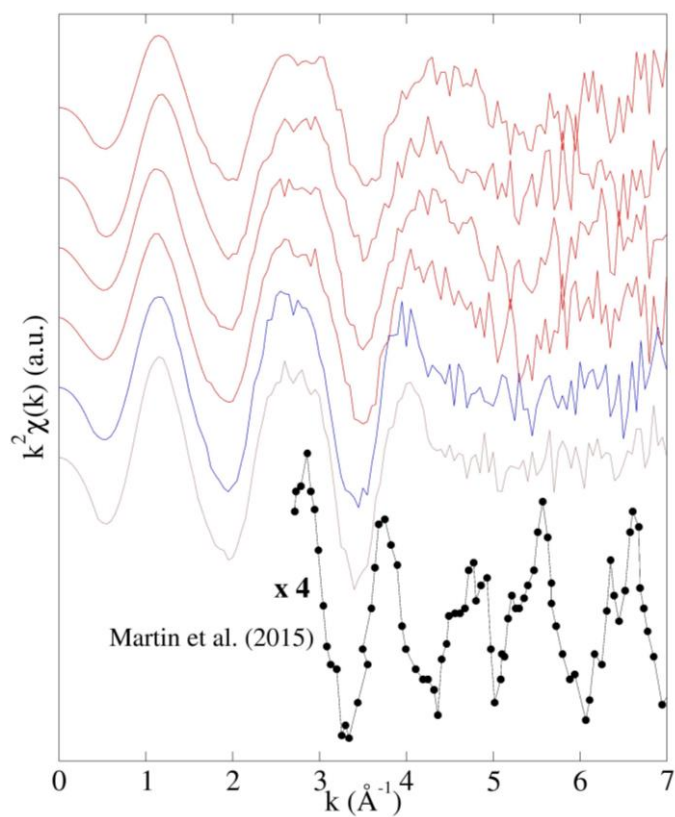659

660

661

662

663

664

665

666

667

668

Figure 4: Magnitude of the Fourier transform of the k^2-weighted Kr EXAFS function without

phase correction (same samples as Figure 3). The peak observed at ~1.9 Å corresponds to

Kr-O = 2.49 Å, and the peak at ~2.9 Å corresponds to Kr-O = 3.32 Å. A general decrease of

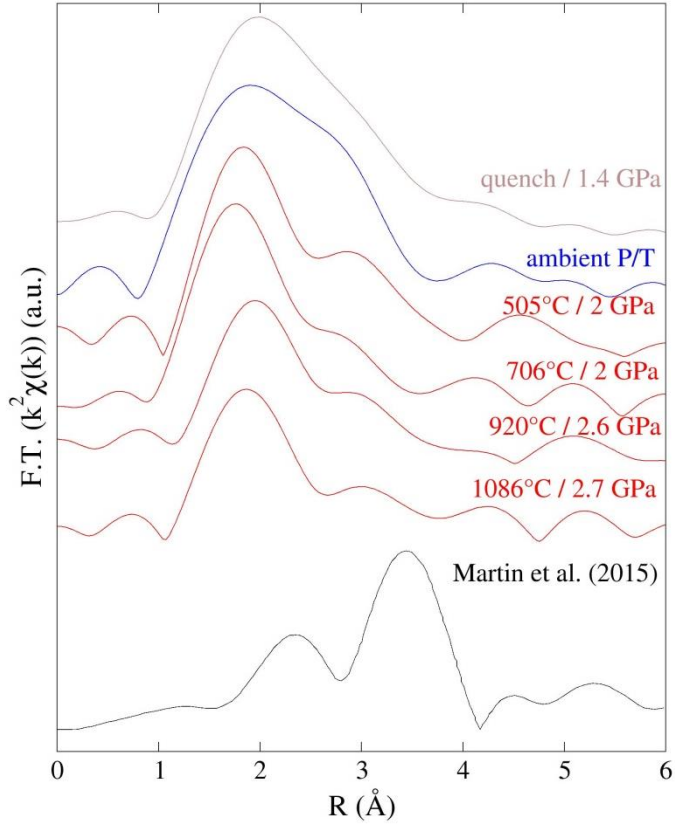*the amplitude is observed with increasing temperature (as noticed by Stern et al., 1991).*

31

684   *Figure 5: Real-part of backward Fourier transform (in dashed lines) and fit to the data (plain*

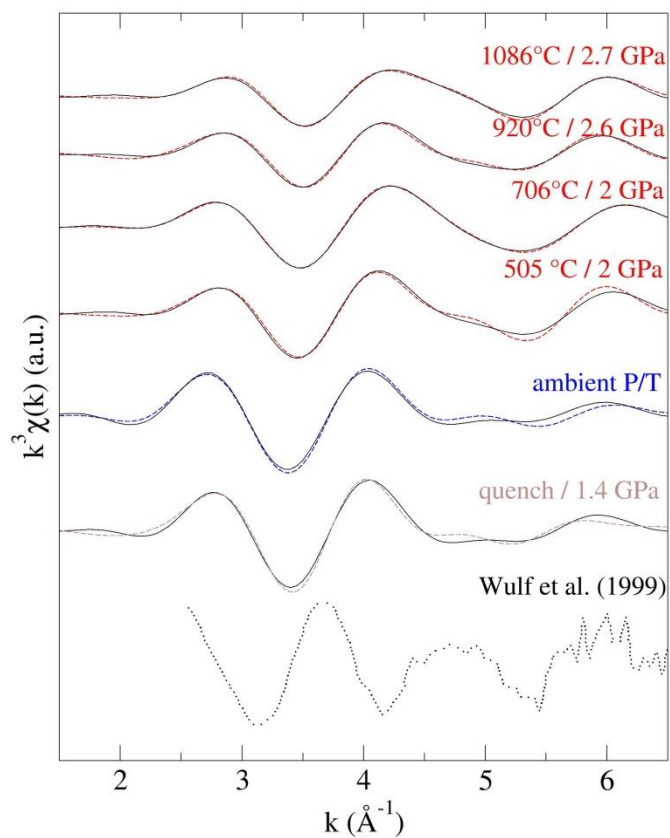685   *black line) for sanidine glass and supercooled liquid, and Kr-bearing SiO₂ glass (Wulf et al.,*

686   *1999).*

687

688

689

690

691

692

693

694

695

696

697

Figure 6: Shift of the Kr K-edge from 1.4 to 2.7 GPa (cf Table 2) compared to the standard

699 *reference value (14326 eV).*

700

701

702

703

704

705

706

707

708

709

710

711

712